International Conference on Space Optics—ICSO 2022

Dubrovnik, Croatia

3–7 October 2022

Edited by Kyriaki Minoglou, Nikos Karafolas, and Bruno Cugny,

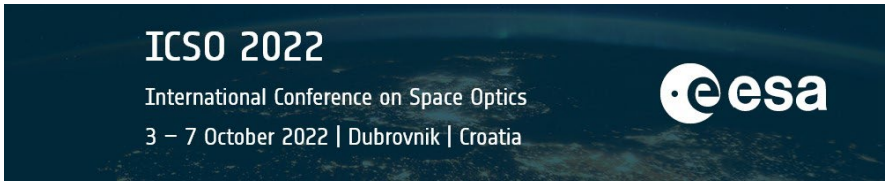

Birefringent interferometer for compact snapshot hyperspectral imaging

International Conference on Space Optics — ICSO 2022, edited by Kyriaki Minoglou, Nikos Karafolas, Bruno Cugny, Proc. of SPIE Vol. 12777, 1277770 · © 2023 ESA and CNES · 0277-786X · doi: 10.1117/12.2691369

Birefringent interferometer for compact snapshot hyperspectral imaging

Matthieu Porte*[a], Elisa Baldit[b], Frédéric Bernard[b], Yann Ferrec [a], Nicolas Guerineau [a]
[a]ONERA, BP 80100, chemin de la Hunière, 91123 Palaiseau, France;
[b]CNES, 18, Avenue Edouard Belin 31400 Toulouse, France

ABSTRACT

Hyperspectral imaging, which consists in imaging a scene at a large number of wavelengths, has several applications, such as mineral identification, target detection, or gas concentration measurement. Most of the remote sensing missions would prefer to have compact instruments, and the ability to measure the information with a single acquisition (snapshot) may also be very interesting. Indeed, the information is not sensitive to the temporal variations of the scene: thus the acquisition of a three-dimensional (x,y,λ) hyperspectral data cubes of fast phenomenon (moving targets/gases) is possible. Furthermore, the hyperspectral image can be used in real time, and snapshot acquisition also reduces constraints on a scanning system.

Among the concepts of "snapshot" hyperspectral imaging, the one proposed by Hirai (Hirai et al., *Optical Review*, 1, 205–207 (1994)) is very interesting. It relies on the association of a microlens array and a Fourier transform interferometer. The latter can be birefringent (Kudenov et al., *Optics express*, *20*(16), 17973-17986 (2012)), which makes the system more compact and less sensitive to vibration by avoiding the use of a beam splitter (as with a Michelson interferometer for instance). Several designs of birefringent interferometers are possible, although the most compact solution is to use a birefringent interferometer with a fringe localization plane at a finite distance and accessible without a relay lens. With such an interferometer, for example a Nomarski prism, the image plane and the plane of localization of the fringes can be easily superposed on a detector.

In this paper, the principle and the parameters that define the spectral/spatial performances of this snapshot hyperspectral imaging design are described. Several scenarios from visible to longwave infrared are presented to highlight the trade-off between spectral and spatial resolution. We then present a study of the propagation of spherical wavefronts through a birefringent interferometer by using 3D simulation and 2D analytical calculation. This tool allows us to quantitatively estimate the impact of the interferometer on the spatial quality of the image (aberration, transverse/axial shift of each channel) and evaluate the real interference pattern and the fringe visibility, i.e. the spectral quality, for the whole field-of-view.

Keywords: Imaging Spectrometer, Fourier Transform, Birefringent interferometer, Birefringent 3D simulation

1. INTRODUCTION

Acquiring hyperspectral image in a single frame enables the acquisition of fast phenomenon (relatively to the whole acquisition time). This can be achieved by using a Fourier Transform interferometer paired with a lenslet array. Hirai et al [1] firstly introduced this concept by using a Michelson interferometer. Latter, Kudenov et al [2] studied a more compact and robust to vibration design, using a birefringent interferometer. The first section presents this design, highlighting the trade-off between the spatial and spectral information. Moreover, it is applied to several scenarios from visible to thermal infrared. The second section, presents different designs of birefringent interferometer that fit this hyperspectral concept. The last section presents a 3D simulation programs that simulate their impacts on the spatial and spectral quality of the hyperspectral image.

1.1 Imaging snapshot hyperspectral Fourier transform spectrometer

The birefringent hyperspectral snapshot optical system is composed of an afocal lens adjusting the focal length of the system, a lenslet array dividing the image of the scene into several subimages on a single focal plane array (FPA), and, between the FPA and the lenslet array, an interferometer. This latter generates interference fringes at an optical path difference (OPD) varying continuously along the plane of the FPA. (Fig.1)

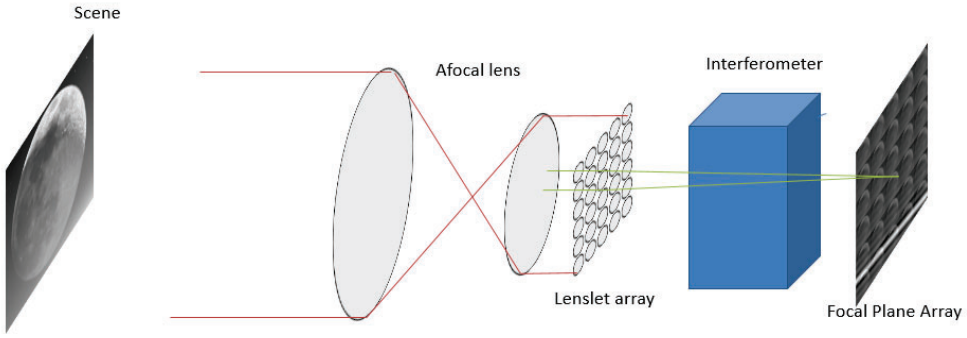

Fig.1 Schematic representation of the proposed snapshot hyperspectral imaging concept.

By dividing the scene into several subimages, the system instantly generates an interferogram for each pixel in the scene (Fig.2). Thanks to the Fourier transform relation between the interferogram and the spectrum, the spectrum for each point of the scene can be reconstructed. Such an optical system can acquire a three-dimensional data cube (x,y,ʎ) image within a single detector acquisition.

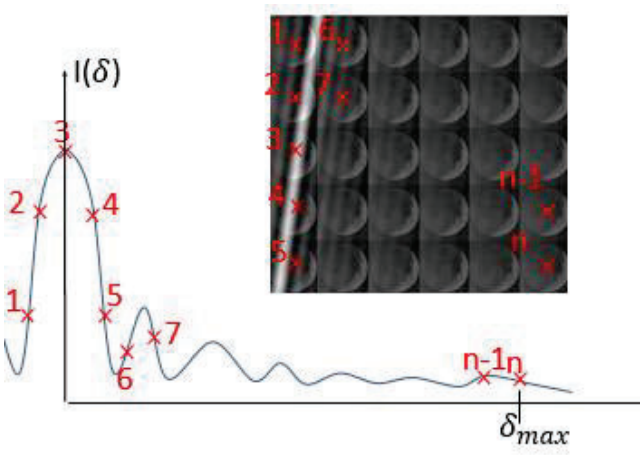

Fig.2 Reconstructed interferogram for 1 point of the scene, from the single frame shown on the top-right insert. Note that the sampling of the interferogram depends on the position of the pixel into the subimage, but with linear and equidistant fringes, the sampling pitch is the same for all the pixels.

1.2 Limitation of the concept

Nevertheless, such an architecture presents limitations and require some trade-off.

For a given spectral band $[\lambda_{min}:\lambda_{max}]$ in wavelength or $[\sigma_{min}:\sigma_{max}]$ in wavenumber, spectral resolution $\Delta\sigma$ in wavenumber, and a detector of $M \times N$ pixels of p_{pix} pitch size, the following parameters are determined:

-The spectral resolution $\Delta\sigma$ is linked to the maximum optical path difference δ_{max} produced by the interferometer: $\delta_{max} = 0.6\frac{1}{\Delta\sigma}$

-The step of optical path difference p_δ (sampling of the interferogram) between two consecutive sub-images must respect Shannon sampling theory $p_\delta < \frac{\lambda_{min}(K+1)}{2}$ with $K = \left\lfloor \frac{\lambda_{min}}{\lambda_{max}-\lambda_{min}} \right\rfloor$ the undersampling factor and $\lfloor\ \rfloor$ the integer part.

-The maximum optical path difference δ_{max} and the optical path step p_δ give the number of sub-images, hence the number of lenslets n is equal to $\frac{\delta_{max}}{p_\delta} > \frac{1.2}{\Delta\sigma\lambda_{min}(K+1)}$.

-The image field of a lenslet is equivalent to its own size. The number of pixels per subimages is then defined by $n_{pix} = \frac{MN}{n} < MN\frac{\Delta\sigma\lambda_{min}(K+1)}{1.2}$.

The three ways to increase the number of pixels per subimages, i.e. the number of spatial pixel of the hyperspectral cube are :

- **Increasing the number of pixels of the detector $M \times N$.**
- **Decreasing the spectral resolution $\Delta\sigma$.**
- **Reducing the spectral band.** (Undersampling can lead to SNR limitation)

There is a clear trade-off between the number of spectral bands and the number of spatial pixels of the hyperspectral cube.

1.3 Scenarios

Here are some examples of scenarios this architecture could achieve with commercial detector (Tab.1). Those are defined by either spatial or spectral needs.

	Spectral bandwidth (µm)	*Spectral resolution (cm-1)*	*Number of spectral bands*	*FPA*	*Number of pixels*	*Pixel size (µm)*	*Number of pixels per subimages*
Visible/NIR (1)	[0.4: 1]	100	150	Thorlabs "CS505MUP - Kiralux "	1024x1224	6,9	64x64
Visible/NIR (2)	[0.5: 0.85]	70	118	Thorlabs "CS505MUP - Kiralux "	1024x1224	6.9	86x86
SWIR (1)	[0.95 :1.65]	65	69	Lynred "SNAKE"	640x512	15	58x58
SWIR (2)	[1.2 : 1.7]	30	82	Lynred "SNAKE"	640x512	15	54x54
MWIR (1)	[0.9 : 3.6]	40	208	Lyrned "SCORPIO"	640x512	15	31x31
MWIR (2)	[3.7 : 4.8]	12	52	Lyrned "SCORPIO"	640x512	15	70x70
LWIR (1)	[7.7 : 9.3]	20	11	Lyrned"SCORPIO LW"	640x512	15	145x145
LWIR (2)	[7.7 : 12]	40	12	Lynred "ATT01280-02"	1280x1024	12	259x259

Tab.1 Imaging snapshot hyperspectral Fourier transform scenarios.

These scenarios highlight the previous point concerning dimensioning limiting points. Between two scenarios targeting the same spectral region, either the spectral bandwidth, the spectral resolution or the number of pixels per subimages are traded to fit the detector dimensions. The first visible/NIR scenario targets a large band to acquire this whole spectral domain, while the second scenario focuses on a smaller spectral bandwidth to study chlorophyll rapid change of reflection (red edge [3]). In the same way, the first SWIR scenario covers the whole [0.95 ; 1.65] µm range, while the second is dedicated to a smaller spectral band, for instance to detect significant CO_2 plumes[4] (despite the lack of the 2 µm band). The first MWIR scenario refers to mineral studies (MIRS [5]) while the second (2) refers to the measurement of jet plumes [6].The LWIR scenarios may be useful for gas detection ([7]), and differ from their detector, with a cooled HgCdTe FPA and a microbolometer FPA.
However, these scenarios need further studies because the interferometer and optical system limitations are not taken into account.

2. INTERFEROMETER

In the following section, we present some types of interferometer that suit this hyperspectral design.

2.1 Interferometers design

In this configuration, the interferometer is placed after the lenslet array, the three mains points to comply with are:

-The optical path difference must be linear within the height of the incident ray.
-The zero path difference must be reached.
-The plane of localization of the fringes must be on the same plane as the image plane, i.e. accessible without a relay lens and parallel to the later.

2.2 Localization plane in imaging configuration

The plane of fringes localization is a key point in the design of the interferometer. One can define it by the plane where the chief rays of the two paths of the interferometer intersect for each lenslet (Fig.3). It is then independent of the position of the lenslet array.

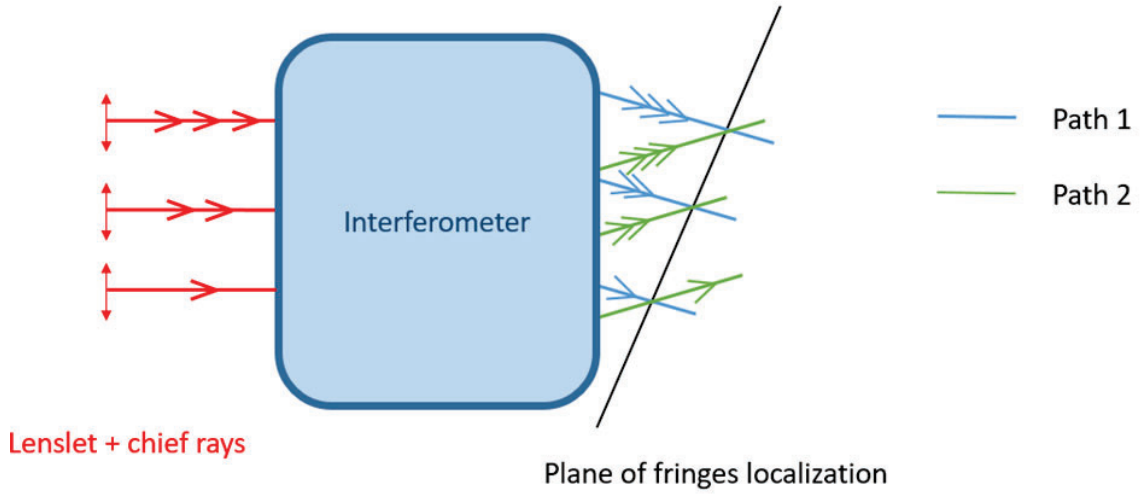

Fig.3 Plane of fringes localization of the interferometer.

On an imaging configuration, the interferometer will produce two images that need to overlap in order to maximize the fringes visibility. These two images may have a transversal displacement *dz* and a lateral one *dy*. The fig.4 describes the influence of the images position in respect to the fringes localization. The closer the images are from the plane of the fringes localization, the closer the lateral gap *dy* is. Hence, the visibility is maximize when the image plane are on the same plane as the plane of fringes localization. Nevertheless, a longitudinal displacement *dz* can remain and lead to geometrical spatial default.

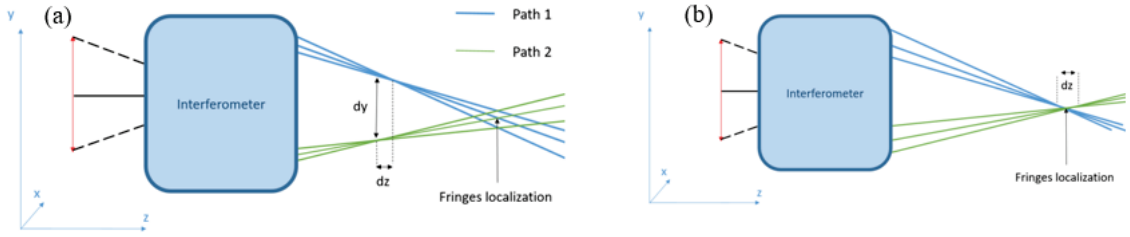

Fig.4 Influence of the image position (directly linked to the lenslet position) compared to the plane of fringes localization. (a) Images are far from the fringes localization; (b) Images are close to the fringes localization.

As a result, it is important to study the position of the fringes localization plane in order to make sure the optical system can focus into it.

2.3 Birefringent interferometer

Using a birefringent interferometer is an advantageous choice thanks to its compactness and robustness to vibration as it is a common path interferometer. The interferometer is made of a combination of prisms, placed between two polarizers (Fig.5). The light is therefore divided into two paths of two linear polarizations corresponding to the eigenmodes of the medium. Throughout the interferometer, each path see either the ordinary index n_o or an extraordinary n_e. It results into an optical path difference between the two paths.

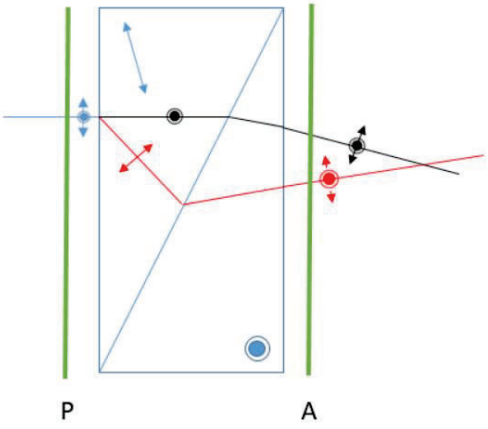

Fig.5 Normaski type interferometer dividing an incident ray into two rays of crossed polarizations. The polarizers (P & A) are oriented at 45° with respect of prisms polarization eigenmodes.

The three points announced in Section 2.1 needs to be respected. The first point is achieved by using prisms. One prism at first order will produce an optical path difference $OPD = (n_e - n_o)e(y)$, with $e(y)$ the thickness of the prism at height y. A small rotation of the interferometer about the z axis, enables to create a varying OPD on the y et x direction. The

second and third points are achieved by using combination of birefringent prisms with different optical axis orientations. Here are some combinations that enable those conditions (Fig.6) :

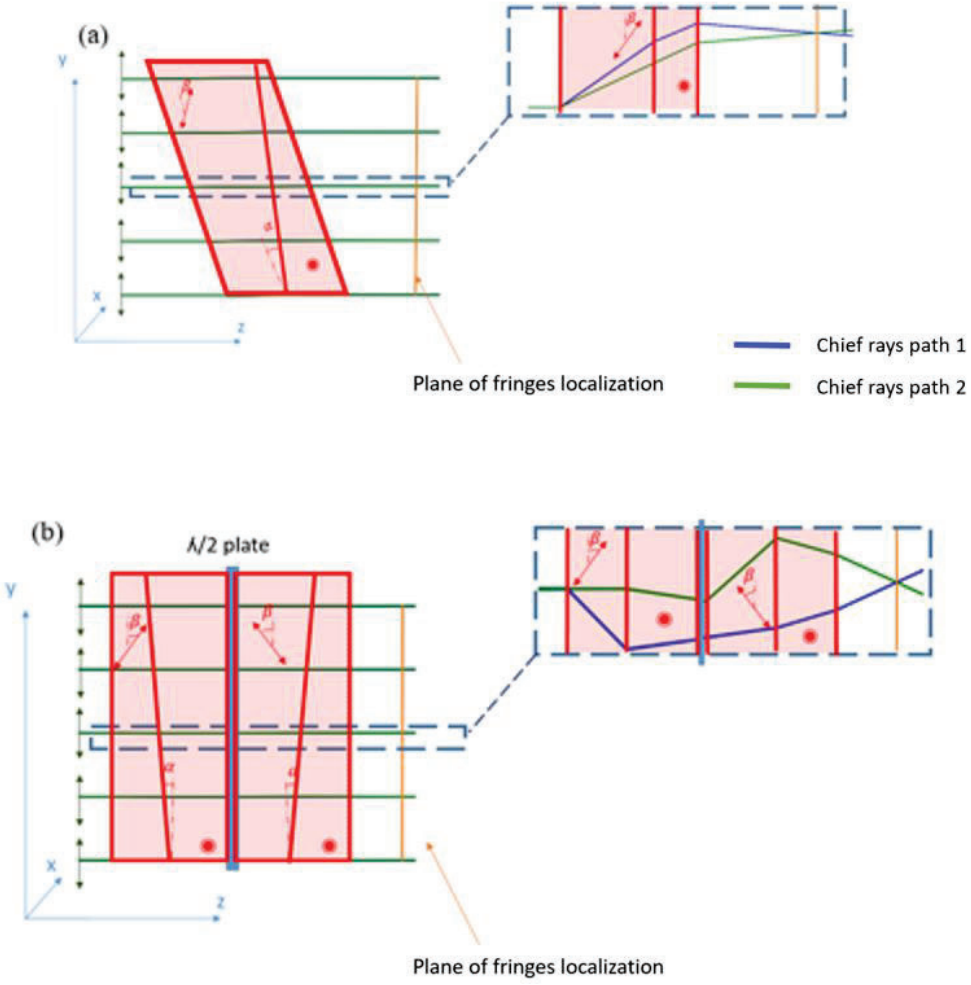

Fig.6 2 combinations of prisms leading to a plane of fringes localization on the image plane. (a) Tilted Nomarski prism [8], (b) Two Nomarski prisms separated by an half-wave plate with axis oriented 45° about the z axis (This plate swaps the polarization along x and y) [2].

3. STUDY OF THE TWO BIREFRINGENT INTERFEROMETERS

3.1 Simulation setup

The goal of the next section is to simulate and compare the 2 previous birefringent interferometers (Fig.6). A Matlab program has been developed in order to evaluate the image quality of the two paths and to evaluate the exact optical path difference seen by a wavefront going through the interferometer. This program was initially developed to simulate plane wavefront propagating through interferometer where the plane of localization is at infinity [9]. As we are using an interferometer that use spherical wavefront, an adjustment has been done in order to propagate an array of rays through it.

The parameters of the two interferometers are taken in order to generate an OPD ranging from 0 to $\delta_{max} = 0.85\ mm$ of the scenario "visible (2)" (Tab.2) and the lenslet is placed in order to focus on the plane of fringes localization. :

	1 tilted Nomarski prism	2 Nomarski prisms + λ/2
OPD, y=[0 : 8.4mm]	$2(n_e - n_o)\tan(\alpha)\, y$	$4(n_e - n_o)\tan(\alpha)\, y$
α	2.6 °	1.3 °
β	5°	5°
Total thickness	5 mm	6 mm
[no , ne] (αBBO @ 800 nm)	[1.661, 1.546]	
Lenslet aperture ϕ (Square lens)	0.6 mm	
Lenslet focal f	8 mm	

Tab.2 Geometrical parameters of the two birefringent interferometers simulated.

3.2 Fringes visibility

For one point of the field coming from one lenslet, each ray composing the spherical wavefront will see different thickness and optical indexes. This will lead to a decrease of the fringes visibility. Moreover, rays between the two paths of the interferometer does not intersect properly on the same plane. It makes difficult to estimate the real optical path difference, i.e. the interference state, on the image plane.

One way to estimate it is to study the monochromatic wavefront of the two paths on the exit pupil. On this plane, the coherent sum of the two wavefronts leads to interference. As the energy is conserved between the exit pupil plane and the image plane, the interference state is unchanged. Then, the normalized interference state for one point of the field can be estimated from there : $I_{interference} =< 1 + \frac{1}{2}\cos(\frac{2\pi}{\lambda}(\delta_1(x,y) - \delta_2(x,y)) >$ with $\delta_1(x,y)$ and $\delta_2(x,y)$ the optical path of the wavefront at the position (x,y) in the exit pupil plane for respectively the first and second path of the interferometer, and "< >" the spatial mean over the pupil plane(Fig.7).

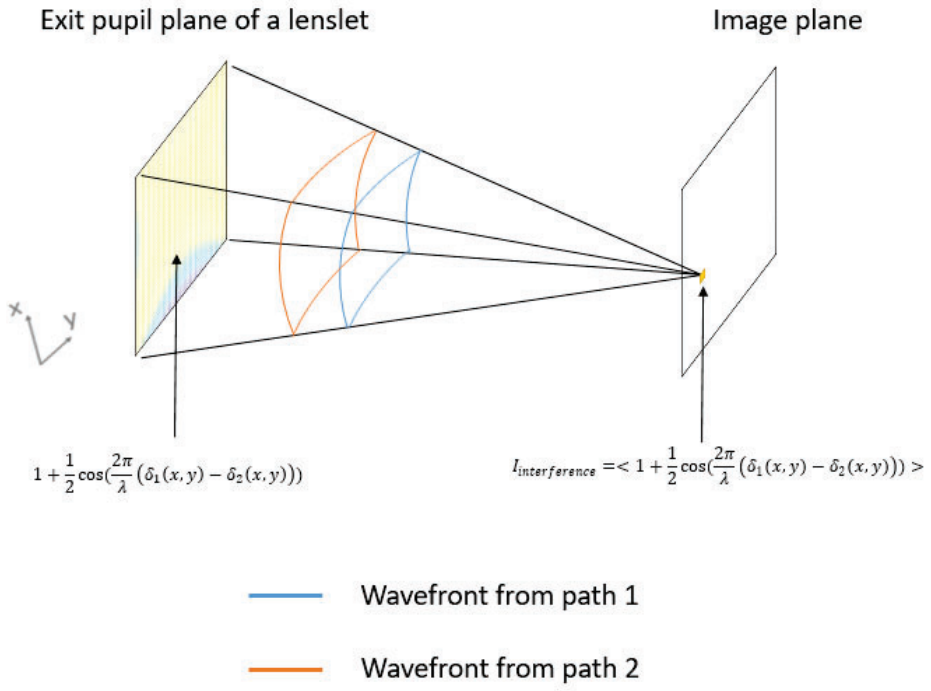

Fig.7 Interference state for one point of the field of one lenslet estimated within the exit pupil plane.

In order to compute it, the optical path on the exit pupil plane is interpolated with the optical path of each ray. For an ideal interferometer, the difference between these two would be constant. Nevertheless, the two paths experienced different aberrations, leading to a non-constant interference state over the pupil (Fig.8&9).

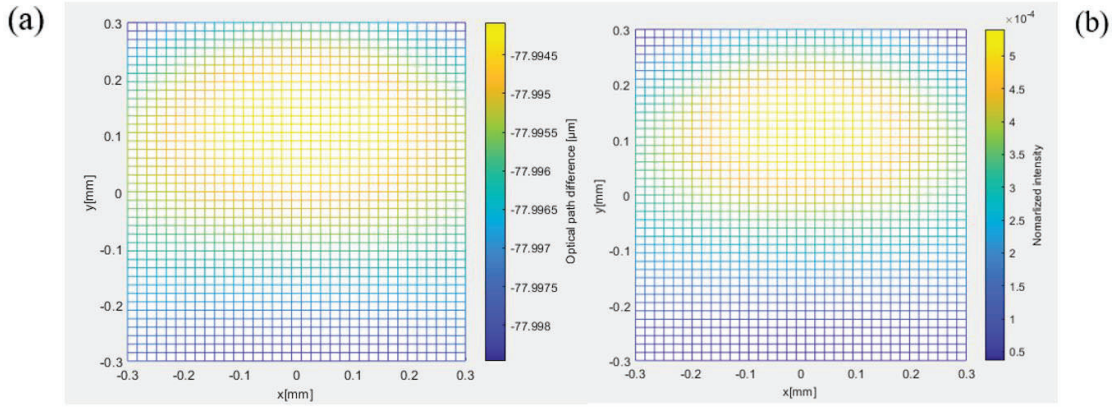

Fig.8 (a) Optical path difference $\delta_1(x,y) - \delta_2(x,y)$ on the exit pupil plane and (b) corresponding normalized intensity defined by $1 + \frac{1}{2}\cos(\frac{2\pi}{\lambda}(\delta_1(x,y) - \delta_2(x,y))$ @ $\lambda = 800nm$ for 2 Nomarski Prisms + $\lambda/2$; The incident wavefront comes from one lenslet centered at a height y = 7.5 mm (destructive state) and focusing on axis.

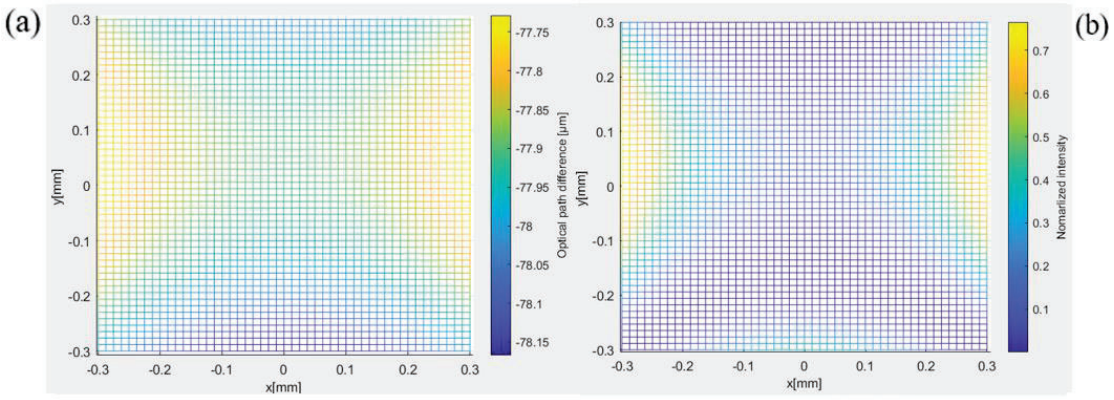

Fig.9 (a) Optical path difference $\delta_1(x,y) - \delta_2(x,y)$ on the exit pupil plane and (b) corresponding normalized intensity defined by $1 + \frac{1}{2}\cos(\frac{2\pi}{\lambda}(\delta_1(x,y) - \delta_2(x,y))$ @ $\lambda = 800nm$ for a tilted Nomaski prism ; The incident wavefront comes from one lenslet centered at a height y = 7.5 mm (destructive state) and focusing on axis.

The interferogram of one lenslet is simulated in the image plane by evaluating the interference state $I_{interference}$ for each point of the field, i.e. by simulating a wavefront converging on each point of the field. As we can see on Fig.8&9, the variation of the difference of optical path on the exit pupil plane is bigger for the tilted Nomarski prism. The resulting interferogram has a lower visibility (Fig.10). One can observe bigger loss of visibility along the field of view, reflecting field aberrations.

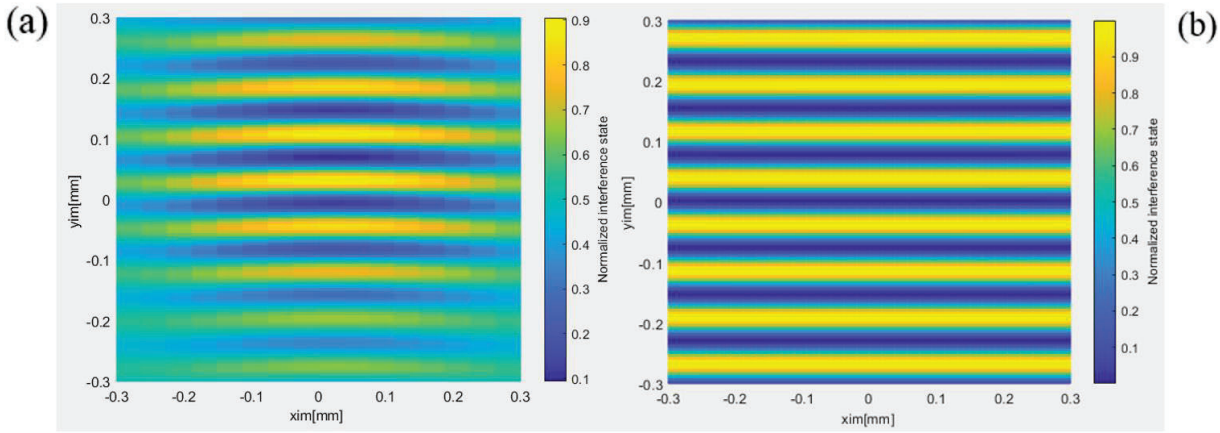

Fig.10 Interferogram in the image plane of one lenslet simulated with the interference state $I_{interference} = < 1 + \frac{1}{2}\cos(\frac{2\pi}{\lambda}(\delta_1(x,y) - \delta_2(x,y)) >$ for each converging wavefront on the image field at $[x_{im}, y_{im}]$. (a) Tilted Nomarski prism (b) 2 Nomarski + ƛ/2; The lenslet is centered at y=7.5 mm; $@\lambda = 800nm$.

For this scenario, the interferometer using a half-wave plate produces an interferogram with a better visibility. Nevertheless, this method only takes into account the difference between the two wavefronts in the exit pupil plane without directly looking into the image spot. Those wavefronts will suffer from optical aberrations and/or diffraction limitation that will lead into a non-stigmatic image.

3.3 Spatial limitation

The spot diagram on the image plane can be simulated in order to look into the spatial quality produced by the interferometer. On Fig.11, the spot diagram on axis of the two interferometers has been simulated. In this case, both produce spot diagrams with a lower size than the diffraction spot : $2\lambda\frac{f}{\phi} \times 2\lambda\frac{f}{\phi}$.

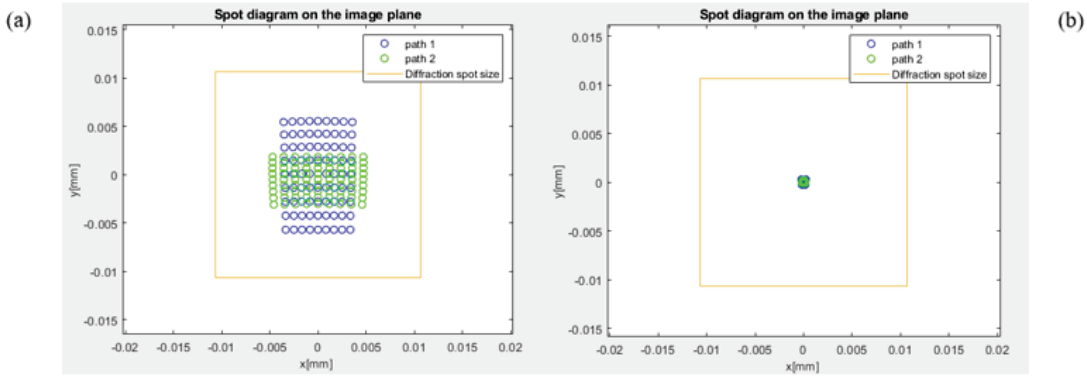

Fig.11 Spot diagrams (Squared aperture @ 800nm) on the image plane produced by the (a) Tilted Nomarski prism (b) 2 Nomarski Prisms + ƛ/2.

However, we notice that the tilted Nomarksi prism produces bigger spot diagrams. This difference comes from the natural focusing shift between the two paths produced by the thickness of the birefringent prisms [10], and due to the anisotropy of the media, wavefront going through extraordinary eigenmodes suffer from astigmatism. This does not affect the spatial quality because the diffraction effect are more important, but they are responsible of the loose of fringes visibility of the previous section. As for the 2nd configuration, using a half-wave plate enables to partially compensate those unwanted effects.

In this scenario, the interferometer using a half-wave plate produces an interferogram with a better fringes visibility because optical aberrations such as difference of focus of the two paths and astigmatism are not significant. On the other hand, those aberrations affect the tilted Nomarski prism. However, it is important to note that those aberrations depend of several parameters such as aperture size, thickness of the interferometer, n_o, n_e. Moreover, the latter is easier to manufacture because the half-wave plate can be difficult to produce for some large bandwidth. It can be necessary to favour this design in some conditions.

4. CONCLUSION

This concept of snapshot hyperspectral imaging can be applied to several scenarios that highlight the trade-off between the spectral and spatial information. Multiple birefringent interferometer designs could theoretically fit this concept. Nevertheless, they can produce spatial and spectral defaults leading to a loss of the hyperspectral information, both from a spectral (fringe visibility) and from a spatial (point spread function) point of view. In order to estimate them, a 3D simulation program enables the study of these interferometers. It simulates the fringe visibility of the interferogram and spatial information for different birefringent interferometers and incident wavefronts, allowing to choose the most appropriate interferometer for a given scenario.

REFERENCES

[1] A. Hirai, T. Inoue, K. Itoh, and Y. Ichioka. ‘Application of Multiple-Image Fourier Transform Spectral Imaging to Measurement of Fast Phenomena’, n.d., 3.

[2] M.W. Kudenov, E.L. Dereniak. ‘Compact Real-Time Birefringent Imaging Spectrometer’. *Optics Express* 20, no. 16 (30 July 2012): 17973.

[3] N. K. Patel, C. Patnaik, S. Dutta, A. M. Shekh, and A. J. Dave. ‘Study of Crop Growth Parameters Using Airborne Imaging Spectrometer Data’. *International Journal of Remote Sensing* 22, no. 12 (January 2001): 2401–11.

[4] W. Di Nicolantonio, A. Tiesi, D. Labate, C. Ananasso, L. Candela, C. Tomasi. ‘On the Evaluation of PRISMA Hyperspectral Satellite Sensitivity to Significant Loadings of Carbon Dioxide’. In *2015 IEEE International Geoscience and Remote Sensing Symposium (IGARSS)*, 3914–16. Milan, Italy: IEEE, 2015

[5] M.A. Barucci, J.M. Reess, P. Bernardi, A. Doressoundiram, S. Fornasier, M. Le Du, T. Iwata, et al. ‘MIRS: An Imaging Spectrometer for the MMX Mission’. *Earth, Planets and Space* 73, no. 1 (December 2021): 211.

[6] Y. Ferrec, S. Rommeluère, A. Boischot, D. Henry, S. Langlois, et al.. High acquisition rate infrared spectrometers for plume measurement. OPTRO 2014, Jan 2014, PARIS, France. Hal-01082099

[7] J.M. Thériault, E. Puckrin, J. Hancock, P. Lecavalier, C. Jackson Lepage, J.O. Jensen. ‘Passive Standoff Detection of Chemical Warfare Agents on Surfaces’. *Applied Optics* 43, no. 31 (1 November 2004): 5870.

[8] C.C. Montarou, T.K. Gaylord. ‘Analysis and Design of Modified Wollaston Prisms’. *Applied Optics* 38, no. 31 (1 November 1999): 6604.

[9] H. Sauer, A. Pola Fossi, Y. Ferrec, N. Guerineau, J. Minet, J. Taboury, P. Chavel. ‘Numerical Modeling of Nominal and Stray Waves in Birefringent Interferometers: Application to Large-Field-of-View Imaging Fourier Transform Spectrometers’. *Applied Optics* 57, no. 31 (1 November 2018): 9488.

[10] M.C. Simon. ‘Image Formation through Monoaxial Plane-Parallel Plates’. *Applied Optics* 27, no. 20 (15 October 1988): 4176